

Weldability of a RS-PM Al-8Fe-2Mo Alloy

Application of high-energy-density welding processes produces three different types of solidification microstructures

BY K. SAMPATH AND W. A. BAESLACK III

ABSTRACT. The weldability of a dispersion-strengthened Al-8Fe-2Mo (wt-%) alloy produced via rapid solidification-powder metallurgy (RS-PM) processing was investigated. Electron beam (EB) and pulsed Nd:YAG laser welding conditions were found to have a significant effect on weld solidification behavior, microstructural development and mechanical properties. Microstructural analysis revealed an influence of local thermal conditions (*i.e.*, temperature gradient and cooling rate), macroscopic solid/liquid interface growth rate and the presence of undissolved/unmelted base metal dispersoid particles on solidification phenomena in the fusion zone. Three different types of solidification microstructures, each of which could be observed to varying degrees within a single weld fusion zone, were observed.

Superior weld mechanical properties, including joint efficiencies of 100% in pulsed Nd:YAG laser welds, were achieved when high energy density welding conditions produced increasingly refined microstructures.

Introduction

In recent years, alloy development efforts based on rapid solidification-powder metallurgy (RS-PM) processing techniques have produced a new generation

K. SAMPATH is with Concurrent Technologies Corp., Johnstown, Pa. W. A. BAESLACK III is with the Department of Welding Engineering, The Ohio State University, Columbus, Ohio.

Originally presented by K. Sampath when a candidate for the Henri Granjon International Award at the 73rd Annual AWS Meeting, held March 22-27, 1992, in Chicago, Ill.

of aluminum alloys for elevated-temperature aerospace applications. These alloys are based on hyper-eutectic Al-Fe compositions with ternary and quaternary additions of transition and rare-earth metals (Refs. 1, 2). These alloy additions exhibit low solid-solubility and low solid-state diffusivity in alpha aluminum (Refs. 3 and 4) and consequently tend to form dispersoid particles. In contrast to conventional ingot metallurgy (IM) processing, rapid solidification processing (RSP) of these novel chemistries suppresses the formation of primary intermetallic particles (Al₃Fe type) and instead produces particulates exhibiting metastable microstructures such as Al-Al₆Fe type micro-eutectic and/or a solute-supersaturated dendritic alpha aluminum. The occurrence of these metastable microstructures is attributed to the following two characteristics of RSP techniques: 1) subdivision of the melt isolates potential nucleants and produces nucleant-free particulates which undergo nonequilibrium solidification (Ref. 5), and/or (Ref. 2) the effect of rapid cooling rate, which does not provide sufficient reaction time for a po-

tential nucleant to produce the equilibrium microstructure (Ref. 6).

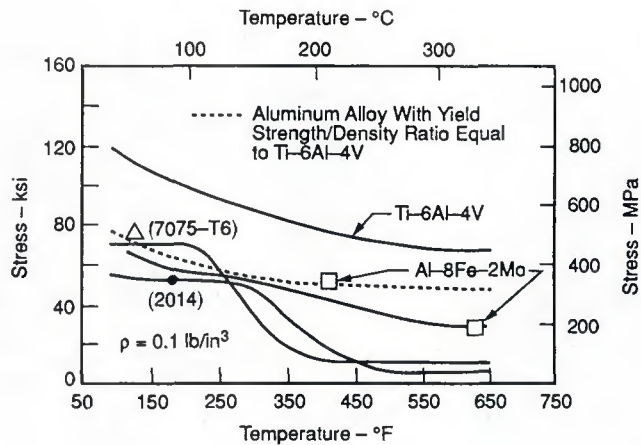
Subsequent thermomechanical processing (TMP) of these rapidly solidified particulates produces a consolidated product with a unique microstructure consisting of submicron-sized dispersoid particles in an extremely fine-grained (<1 μm) alpha aluminum matrix. These microstructural features provide dispersion strengthening (Refs. 2, 4 and 6), and exhibit high specific strength at elevated temperatures up to 345°C (650°F). In fact, a comparison of the elevated-temperature tensile yield strengths of a dispersion-strengthened RS-PM Al-8Fe-2Mo alloy with conventional IM alloys used in aerospace applications (Fig. 1) indicates that the Al-Fe based alloy exhibits high specific strength comparable to Ti-6Al-4V. In view of their superior properties, these Al-Fe based alloys produced via RS-PM processing are considered candidate materials to replace titanium alloys used in the fabrication of several aerospace components such as fan and compressor cases, vanes and blades in gas turbine engines and fins, winglets and rocket motor cases of missiles (Refs. 6, 7) which operate at elevated temperatures up to 345°C (650°F). The substitution of RS-PM Al-Fe based alloys is expected to allow significant improvements in the thrust-to-weight ratio and the performance characteristics of these aerospace components.

Since weight savings are critical for advanced aerospace structural applications, joining of these RS-PM Al-Fe based alloys requires the utilization of welding processes and/or conditions that can produce high joint efficiency without an appreciable increase in weld size or re-

KEY WORDS

Electron Beam Welding
Pulsed Nd:YAG Laser
Laser Welding
Powder Metallurgy (PM)
Rapid Solidification
Al-8Fe-2Mo Alloy
Weld Microstructure
Weld Solidification

Fig. 1 — A comparison of elevated-temperature tensile yield strengths of dispersion-strengthened RS-PM Al-8Fe-2Mo alloy with conventional IM alloys for aerospace applications (Ref. 2).



inforcement. Further, considering the relationships between the unique microstructure and the superior mechanical properties of the RS-PM base material, weldability considerations require utilization of welding processes and/or conditions which can "recreate" a rapidly-solidified microstructure and/or "retain" the high performance base metal microstructure in the weld zone. An earlier investigation involving the metallographic characterization of an electron beam (EB) weld in a RS-PM Al-8Fe-1.7Ni alloy showed that the rapid-solidification and cooling conditions associated with the high energy density EB welding process offered a strong potential for "recreating" a rapidly solidified microstructure in the fusion zone (Ref. 8). However, a relatively high hydrogen content (>5 mL/100 g of Al) of the base metal resulted in excessive fusion zone porosity and precluded evaluation of microstructure/mechanical property relationships.

The present weldability investigation utilized a low-hydrogen (<1 mL/100 g

of Al) RS-PM Al-8Fe-2Mo alloy in order to evaluate the effects of weld process conditions on the development of fusion zone microstructure and weld mechanical properties.

Objectives

A comparison of the rapid solidification conditions which produce metastable microstructures in RSP particulates with weld fusion zone solidification conditions reveals significant differences. These differences arise mainly from the following characteristics of a fusion weld:

- 1) the presence of a readily wettable base metal substrate;
- 2) the presence of oxide impurities which can serve as heterogeneous nucleating agents in the fusion zone;
- 3) an absence of any nucleant isolation effect (Ref. 5) in the weld fusion zone.

In view of the above differences, the present investigation was aimed at de-

Table 1 — Mechanical Properties of RS-PM Al-8Fe-2Mo Sheet

UTS, Longitudinal ^(a)	510 MPa (74 ksi)
% Elongation	14
UTS, Transverse ^(b)	376 MPa (54.5 Ksi)
% Elongation	11

(a) Average of 3 values (500, 512, 518)

(b) Average of 3 values (366, 388, 374)

veloping a fundamental understanding of the influence of welding process and parameters on the solidification behavior of representative EB and pulsed Nd:YAG laser welds in an RS-PM Al-8Fe-2Mo alloy via detailed microstructural characterization and to correlate this behavior with welding conditions and parameters. The pulsed Nd:YAG laser welding process was utilized in this investigation as this process provided 1.06 μm wavelength radiation, which is more efficiently absorbed by aluminum and its alloys compared to 10.6 μm wavelength CO₂ laser radiation. From a broader perspective, this investigation was also purposed to facilitate a fundamental understanding of microstructural development in the weld fusion zone in advanced structural materials such as particulate reinforced metal-matrix composites (MMC) and intermetallic matrix composites (IMC) which obtain strengthening from the presence of high melting point dispersoid particles.

Experimental Procedure

The Al-8Fe-2Mo alloy (actual chemistry: 8.0 wt-% Fe and 2.3 wt-% Mo) studied in this investigation originated as rapidly-solidified powder produced by Pratt and Whitney's rapid solidification rate (RSR) process. In the RSR pro-

Table 2 — Welding Parameters and Weldment Characteristics of Al-8Fe-2Mo Sheet

Weld #	Travel Speed mm/s	Energy Input J/mm	Threshold Bending Strain %	Transverse-Weld Tensile Test			
				UTS MPa (Ksi)	EL %	Failure Location	Joint Efficiency %
EB Welding ^(a) (weld oriented transverse to the rolling direction)							
1	12.7	27.6	3.3				
2	14.8	23.6	3.3				
3	16.9	23.6	4.0	330 ^(d) (46.5)	1.6	FBR	65
4	16.9	20.7	4.0				
5	23.3	19.3	4.0	370 ^(e) (53.5)	5.6	FBR	73
6	19.1	18.4	4.0				
7	21.2	16.5	4.0				
8	23.3	15.0	5.0				
Pulsed Nd:YAG Laser Welding ^(b) (weld oriented along the rolling direction)							
9	2.5	41.3 ^(c)	11.0	374 ^(f) (54.2)	11	UBM	100

(a) EB Welds Nos. 1 to 8, acceleration voltage: 100 kV, current: 3.5 mA except for No. 3 (4.0 mA) and No. 5 (4.5 mA).

(b) 10 Hz pulse rate, 5.0 ms pulse duration, 105 W pulse power (10.5 J/pulse), 2.1 kW peak power, 102 mm focal length, ≈10⁶ W/mm² power density, 16.5 L/min argon shielding gas flow rate.

FBR — fusion boundary region; UBM — unaffected base metal.

(c) Average energy input.

(d) Average of 4 values (342, 320, 326, 332).

(e) Average of 4 values (368, 370, 376, 366).

(f) Average of 4 values (370, 370, 379, 376).

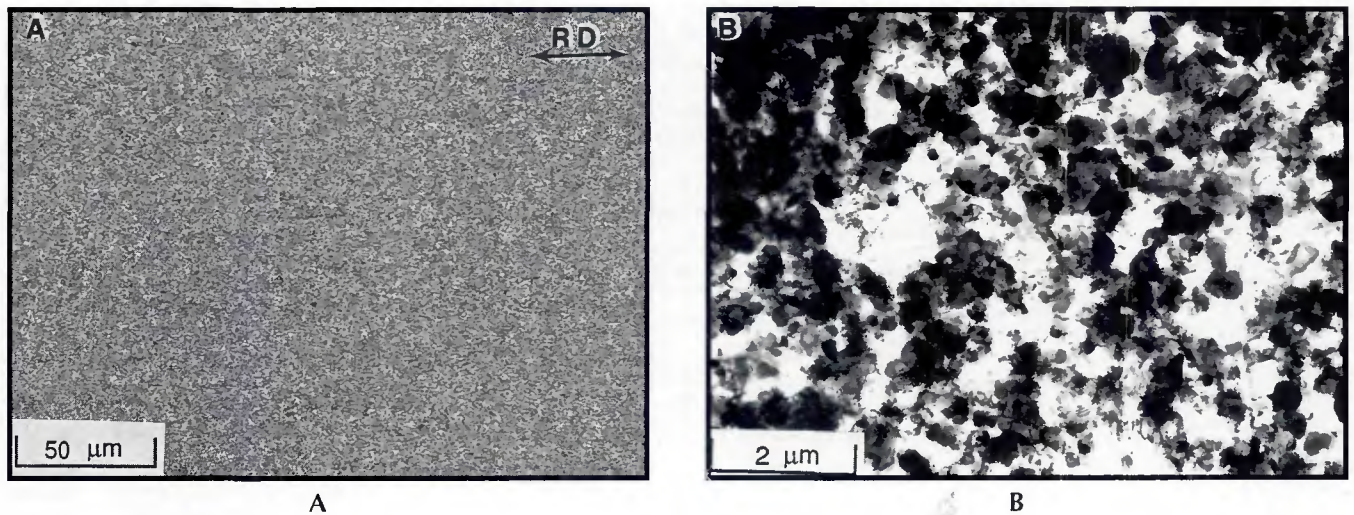


Fig. 2 — A — Light micrograph; B — TEM micrograph of the as-received 1.27-mm Al-8Fe-2Mo sheet. Arrow in A indicates rolling direction.

cess, a rapidly spinning disk disperses a homogeneous melt of uniform chemical composition into fine, spherically symmetric powder particles by centrifugal atomization (Ref. 9). A high velocity (100 m/s) helium gas jet utilized in conjunction with the rapidly spinning disk provides convective cooling under chemically inert conditions. The inert atomization conditions minimize surface oxidation and reduce subsequent hydration of the powder particles, thereby enabling production of a base alloy with a minimal hydrogen content. From a solidification standpoint, the helium shroud provides a steep temperature gradient in the range from $10^{3^{\circ}}$ to $10^{4^{\circ}}$ C/mm across the powder particle and depending on the powder particle size generates liquid cooling rates in the range of $10^{4^{\circ}}$ to $10^{6^{\circ}}$ C/s (Ref. 4). These rapid solidification conditions produce a micro-eutectic (Al-Al₆Fe type) or solute-supersaturated dendritic alpha aluminum structure in the individual powder particulates (Refs. 4, 6). Subsequent inert compaction of the powder and TMP (extrusion followed by warm rolling) produced sheet 1.27 mm in thickness. Table 1 shows selected mechanical properties of 1.27-mm thick RS-PM Al-8Fe-2Mo sheet.

Autogenous, full-penetration EB and pulsed Nd:YAG laser welds were produced in the 1.27-mm thick Al-8Fe-2Mo sheet. Table 2 shows the specific EB and pulsed Nd:YAG laser welding parameters. The EB welding conditions typically employed a power level of 3.5 kW to 4.5 kW. Although the pulsed Nd:YAG laser welding conditions employed a lower power level (peak power of 2.1 kW), the sharp focus conditions produced a higher power density ($\sim 10^6$ W/mm²) compared to the EB welding. A second Nd:YAG laser weld was produced at a higher power level (4.6 kW

peak power, 230 W pulse power, or 23 J/pulse) in an overlapping spot mode (about 40% overlap) to provide enhanced delineation of solidification microstructures.

Following radiographic inspection, the weld coupons were sectioned and the transverse sections were mounted in epoxy, ground to 600 grit emery, and polished with a 3- μ m diamond compound followed by a final polish using a colloidal silica suspension. In order to examine the effects of successive laser pulses on the development of fusion zone microstructures, the top section of the pulsed Nd:YAG laser welds was also prepared for metallographic characterization. The metallographic samples were etched using Keller's reagent (2.5 mL HNO₃ + 1.5 mL HCL + 1 mL HF + 95 mL distilled water) for characterization using light microscopy and scanning-electron microscopy (SEM).

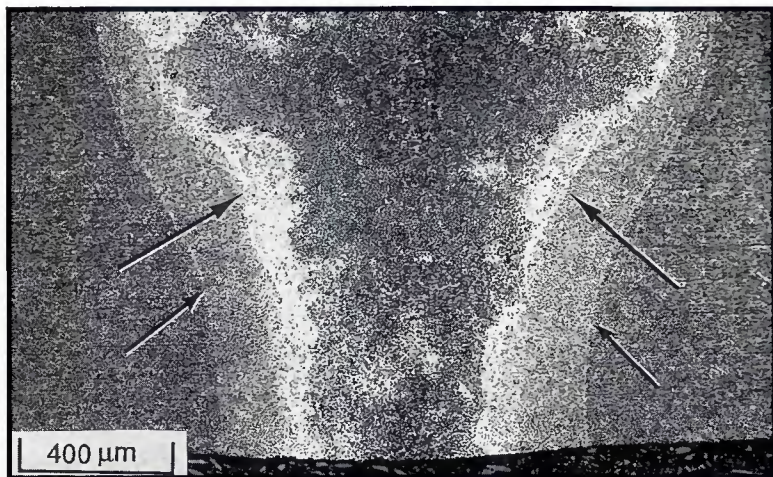
Base metal and representative weld coupons were also characterized using transmission-electron microscopy (TEM). Thin foils for TEM characterization were prepared by a twin-jet electropolishing technique using a solution of 1 part nitric acid in 3 parts methanol, at 20 V and at a temperature of -25° C. TEM characterization mainly involved amplitude contrast imaging under bright-field (BF) and dark-field (DF) imaging conditions and was performed using a JEOL 200CX microscope operated at 200 kV. The bright-field and dark-field imaging conditions were employed mainly to estimate the alpha aluminum grain size and the size of the second-phase particles and to recognize the weld solidification growth morphologies. In addition to the amplitude contrast imaging, microchemical analysis was carried out in the scanning-transmission-electron microscopy (STEM) mode using a Tracor-Northern TN2000

energy-dispersive spectrometer (EDS) system equipped with a beryllium window detector at a 72-deg take-off angle. A Cliff-Lorimer data analysis algorithm based on empirically determined K factors (Ref. 10) was utilized to obtain semi-quantitative compositions from EDS data. These semi-quantitative compositions were utilized in conjunction with the published data on Al-Fe-based alloys and Al-Fe and Al-Mo binary systems in order to elucidate the solidification behavior of the weld fusion zone. Identification and determination of the crystal structure of the individual phases in the fusion zone and determination of the orientation relationships between the individual phases were not within the scope of the current investigation.

Following light microscopy examination, Vickers microhardness (DPH, 500-g load) traverses were obtained from the transverse sections of the EB welds and from the transverse and top sections of the pulsed Nd:YAG laser weld. In order to correlate microstructure with weld mechanical properties a limited mechanical property testing of the weldments was also performed. This included transverse-weld-oriented tensile testing of selected weldments (Nos. 3, 5 and 9 in Table 2) and longitudinal-weld-oriented bend testing of sections of all weldments. Longitudinal-weld-oriented bend testing was performed with the weld face in tension and the threshold bending strain (minimum strain to cause cracking) was determined using the following relationship:

$$\epsilon = t/(2R + t) \quad (1)$$

where: ϵ is the outer fiber strain, t is the thickness of the test coupon and R is the radius of the die-block used for bending.



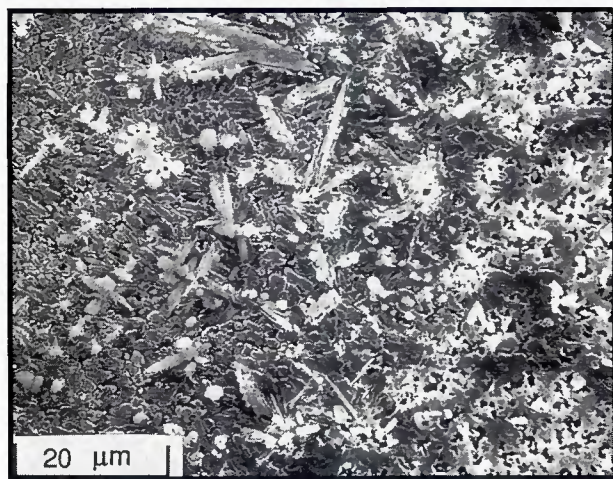
A

Fig. 3 — EB weld (energy input 15 J/mm) in Al-8Fe-2Mo sheet:

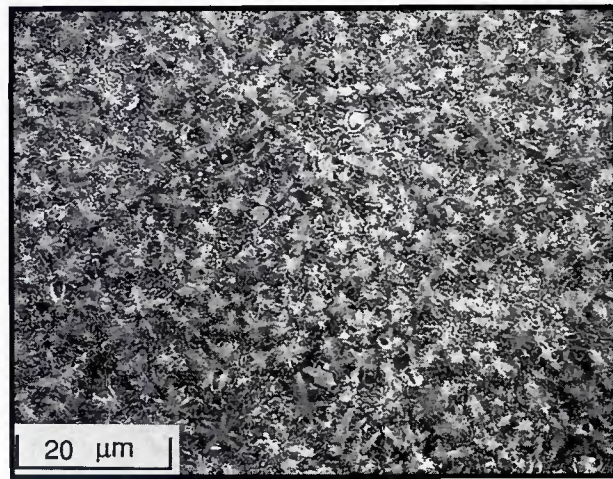
A — macrostructure, large arrows indicate fusion boundary, small arrows indicate HAZ bounding fusion zone;

B — microstructure near the fusion boundary;

C — microstructure near weld center.



B



C

Results and Discussion

Base Metal Characterization

Light microscopy examination of the as-received Al-8Fe-2Mo sheet oriented parallel to the rolling direction showed a uniform distribution of fine-sized, dark-etching dispersoid particles in a light-etching alpha aluminum matrix — Fig. 2A. Dark-etching stringers were also occasionally observed along the rolling direction. These stringers appeared to originate from coarse powder particles which contained appreciable coarse-sized primary intermetallic particles (Ref. 3). Boundaries between individual powder particles were not evident indicating the effectiveness of the thermo-mechanical processing treatment. Consistent with the complete inert RSR and TMP treatments, the microstructure did not show significant oxide stringers.

TEM examination of thin foils from the Al-8Fe-2Mo base alloy revealed a uniform distribution of submicron-sized dispersoid particles in a fine-grained alpha aluminum matrix — Fig. 2B. Bright-field and dark-field imaging indicated the alpha aluminum grain size to

range from 1 to 2 μm. Semiquantitative STEM/EDS analysis of the base metal alpha aluminum grains indicated appreciable supersaturation of both Fe (~0.35 wt-%) and Mo (~0.7 wt-%) relative to the equilibrium maximum solid solubility limit of both Fe (0.04 wt-%) and Mo (0.25 wt-%) in alpha aluminum (Refs. 11, 12). Additionally, TEM observations indicated the dispersoid particles to typically exhibit either a spherical (polygonal) or an acicular morphology. In view of the submicron size of these particles, the specific dispersoid types could not be identified using selected-area electron diffraction techniques. However, STEM/EDS compositional analysis indicated that the spherical dispersoids were enriched in both Fe (~18 wt-% or 10.25 at.-%) and Mo (~8.3 wt-% or 2.75 at.-%). These spherical particles were likely Al₆Fe type, which is a metastable, partially coherent strengthening intermetallic previously reported in RS Al-Fe-Mo and Al-Fe alloys (Ref. 3). STEM/EDS analysis of the acicular particles indicated a relative increase in Fe content (~30 wt-% or 17.38 at.-%) and a significant decrease in Mo content (~1.5 wt-% or 0.52 at.-%). These particles pre-

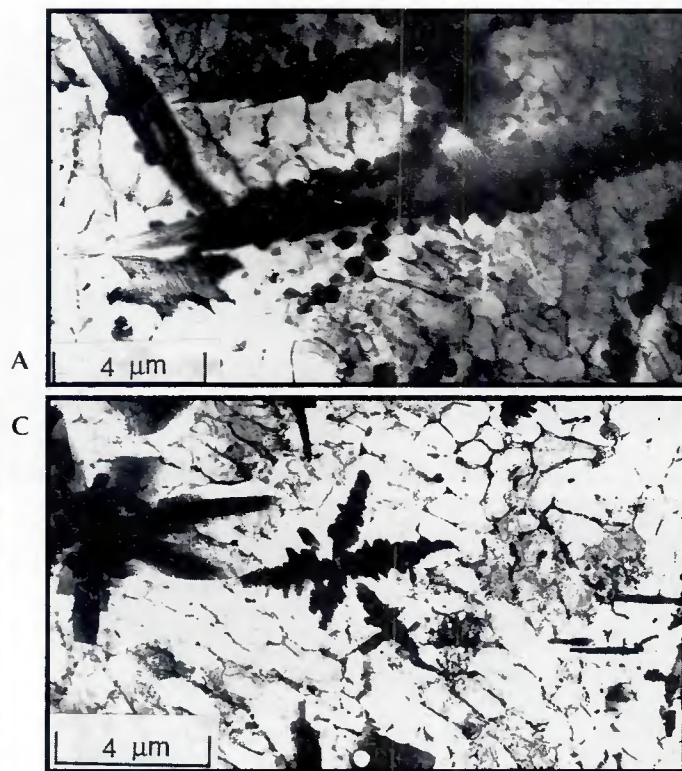
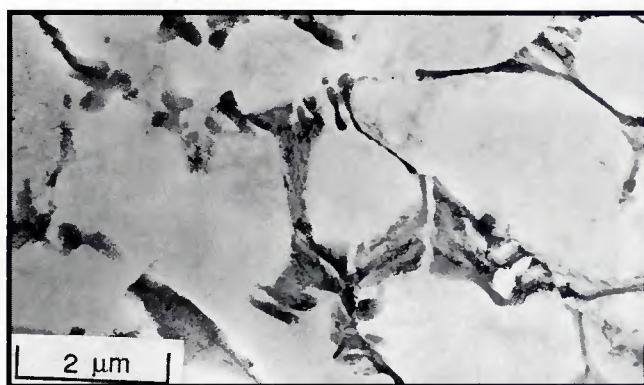
sumably belonged to the equilibrium θ-Al₃Fe or Al₁₃Fe₄ type intermetallics (Refs. 3, 11).

Weld Structure Characterization

Electron Beam Weldments

Light microscopy examination of EB welds showed a moderate depth-to-width ratio FZ comprised of a light-etching region near the fusion boundary, and a relatively uniform, dark-etching region in the central fusion zone, and a noticeable HAZ outside of the fusion boundary. Figure 3A shows the macrostructure of EB weld No. 8. SEM examination of the light-etching fusion boundary region (FBR) at increased magnification revealed second-phase particles exhibiting an acicular (high aspect-ratio) morphology, randomly oriented in a matrix of relatively coarse-sized dendritic alpha aluminum (Fig. 3B). Occasional, fine spherical particles were also observed in this region. SEM examination of the dark-etching region within central fusion zone showed fine-sized second-phase particles exhibiting an equiaxed morphology, uniformly dis-

Fig. 4—TEM micrographs of EB weld (energy input 15 J/mm) in Al-8Fe-2Mo. A — Acicular Al_3Fe type intermetallic particles and dendritic alpha aluminum matrix; B — interdendritic Al_6Fe type metastable lamellar eutectic in the light-etching fusion boundary region; C — equiaxed Al_3Fe type intermetallic particles and solute-rich particles in alpha aluminum interstices in the dark-etching central fusion zone.



persed in a fine-sized dendritic alpha aluminum matrix (Fig. 3C). In addition to the difference in the morphology of the second-phase particles, the weld center showed a significant increase in the population of second-phase particles vs. the fusion boundary region.

TEM examination of the light-etching FBR confirmed the presence of acicular particles in a matrix of coarse-sized dendritic alpha aluminum — Fig. 4A. The size of the alpha aluminum dendrites was approximately 2 μm . STEM/EDS analysis of the alpha aluminum dendrites revealed appreciable supersaturation at ≈ 0.42 wt-% Fe (0.20 at.-%) and ≈ 0.76 wt-% Mo (0.21 at.-%) relative to the equilibrium solid solubility limits of both Fe and Mo in alpha aluminum (Refs. 11, 12). STEM/EDS analysis of the acicular particles showed ≈ 29.2 wt-% Fe (16.84 at.-%) and ≈ 1.6 wt-% Mo (0.54 at.-%), indicating these particles were likely Al_3Fe type intermetallic. TEM examination also revealed the occasional presence of fine-sized spherical particles in this region. STEM/EDS analysis of these spherical particles indicated that they were likely Al_6Fe type. TEM examination of the alpha aluminum dendrite interstices showed a fine-sized lamellar eutectic microstructure — Fig. 4B. STEM/EDS analysis of the interlamellar particles showed a typical composition of ≈ 19.4 wt-% Fe (10.94 at.-%) and ≈ 6 wt-% Mo (1.97 at.-%), indicating an Al_6Fe type metastable intermetallic.

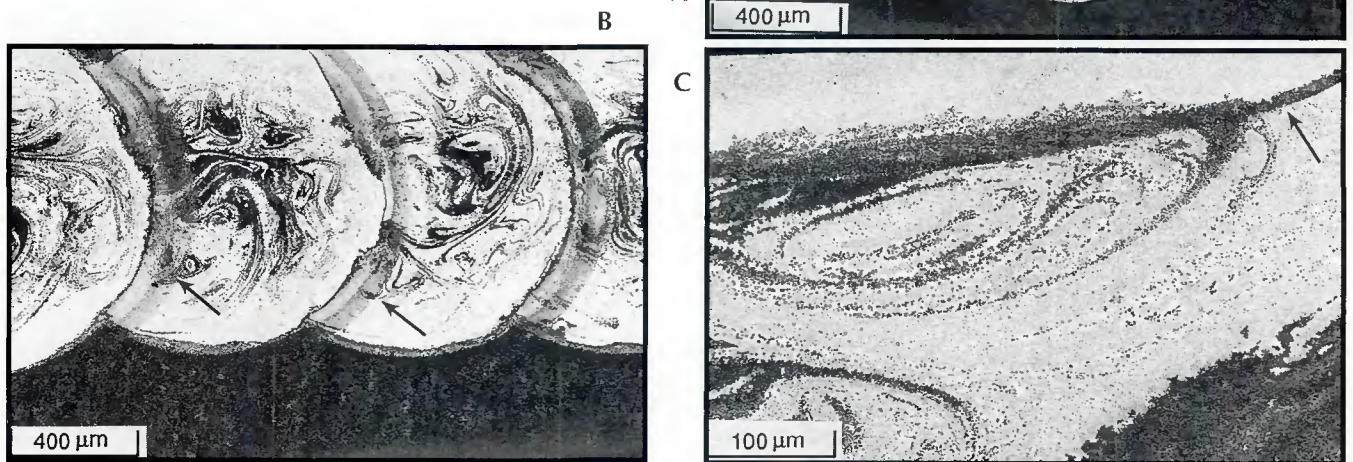
TEM examination of the dark-etching central fusion zone showed coarse-sized equiaxed-dendritic particles in a fine-grained dendritic alpha aluminum matrix, and solute-rich particles at the alpha dendrite interstices — Fig. 4C. The side arms of the coarse-sized intermetallic particles were about 2 μm in length, and the size of the alpha aluminum cells ranged from about 0.5 to 1 μm . STEM/EDS analysis showed the well-developed equiaxed particles contain typically ≈ 26.7 wt-% Fe (15.3 at.-%) and ≈ 2.9 wt-% (0.97 at.-%) Mo indicating that the particles were likely Al_3Fe type. TEM examination using BF and DF imaging did not indicate any orientation relationship between the equiaxed intermetallic particles and the dendritic alpha aluminum matrix. The size of the solute-rich particles at the alpha aluminum dendrite interstices was in the range of 0.1 to 0.2 μm .

Correlation of the alpha aluminum dendrite spacing in the central weld fusion zone with previous dendrite arm spacing/cooling rate relationships for aluminum alloys (Refs. 13, 14) indicated a weld cooling rate between 10^3 and 10^4 $^\circ\text{C}/\text{s}$. It is interesting to note that although the use of such moderately rapid fusion zone cooling rates facilitated marginal substitution of Mo atoms for Fe atoms within the intermetallic particles, the growth of equilibrium Al_3Fe type intermetallic particles could not be suppressed within the bulk fusion zone. Further, although the RS-PM

Al-8Fe-2Mo base metal contained Al_6Fe type dispersoid particles, the EB weld fusion zone did not show significant evidence for the presence of Al_6Fe type intermetallic particles.

The metallographic examination of the other EB welds (Nos. 1–7 in Table 2) did not show appreciable differences in either the type or the morphology of the microstructural constituents in the fusion zone compared to weld No. 8, although the proportion of light-etching to dark-etching microstructural regions, and the width of the HAZ generally increased with an increase in weld energy input. It is of importance to note that the coarse fusion boundary structure exhibited by EB welds in this Al-8Fe-2Mo alloy contrasted previous results on the FZ microstructure of a high depth-to-width ratio EB weld in 25.4-mm (1-in.) thick Al-8Fe-1.7Ni alloy (Ref. 8), which found epitaxial solidification to a Al- Al_6Fe type micro-eutectic structure, and a gradual increase in the size and quantity of equilibrium Al_3Fe type intermetallics toward the weld center. The occurrence of the micro-eutectic structure in the Al-8Fe-1.7Ni alloy was attributed to the extremely steep temperature gradient and rapid cooling rates experienced near the fusion line for the high depth-to-width ratio EB weld (Ref. 8). The absence of such microstructures in the FZ of EB welds in the Al-8Fe-2Mo sheet is attributed to the effects of shallow temperature gradient (as indicated by the wide widths of the HAZ in these

Fig. 7 — Microstructure of pulsed Nd:YAG laser weld (overlapping spot welds) in Al-8Fe-2Mo sheet. A — Transverse section; B — top surface; C — transverse section showing top corner of fusion zone. Small arrows indicate HAZ bounding successive melt zones. Dark-etching swirls correspond to dispersoid coarsened regions.



HAZ microstructures. TEM observations of the light-etching FBR (near the outer periphery of the weld with the base metal) using BF and DF imaging conditions revealed fine-sized spherical particles and epitaxial growth of columnar-dendritic alpha aluminum from base metal alpha aluminum grains — Fig. 8A. The size of the individual alpha aluminum dendrites was about 2 μm. STEM/EDS analysis found the spherical particles within the columnar alpha alu-

minum dendrites to typically contain 17.1 wt-% Fe (9.72 at.-%) and 8.7 wt-% Mo (2.87 at.-%), indicating these were likely Al₆Fe type intermetallics. The fine size and spherical morphology of these intermetallics and their Al₆Fe type composition suggested their origin from the base metal.

Figure 8B shows the light-etching region of the fusion zone, which consists of spherical particles in a matrix of extremely fine dendritic alpha, or possibly

a microeutectic. As near the fusion boundary, the Al₆Fe composition of these particles, and their size and morphology suggested their possible origin from the base metal.

The dark-etching central FZ regions exhibited relatively coarse-sized particles which nucleated grains of dendritic alpha aluminum — Fig. 8C. STEM/EDS analysis of the coarse-sized particles revealed the composition as ≈23.8 wt-% Fe (14.1 at.-%) and ≈8.25 wt-% Mo (2.8

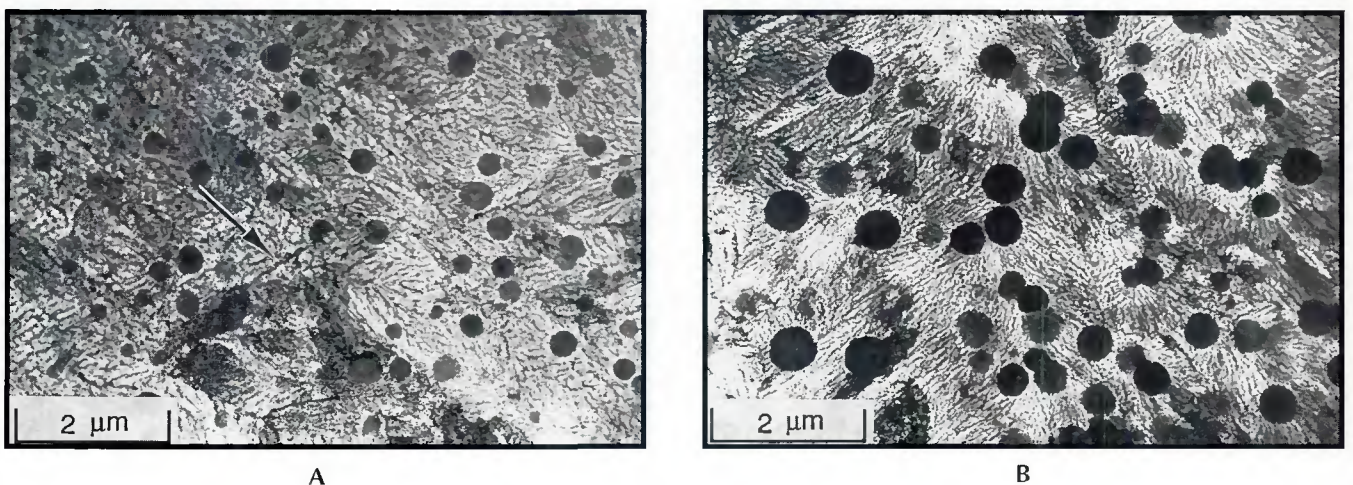


Fig. 8 — TEM micrographs of pulsed Nd:YAG laser weld (overlapping spot welds) in Al-8Fe-2Mo sheet: A — FBR adjacent to base metal; B — FZ (light-etching regions in Fig. 7); (continued on next page)

coarse-sized intermetallic particles in the fusion boundary region. These particles appeared to promote strain localization and preferential sites for crack initiation.

Evaluation of the mechanical properties of the pulsed Nd:YAG laser weld (No. 9 in Table 2) showed excellent correlation with the metallographic analysis. Transverse-weld tensile testing found fracture to occur in the unaffected base metal, indicating 100% joint efficiency and a transverse-weld tensile strength of 374 MPa (54.2 ksi). Microhardness traverses across the weld showed hardnesses in the light-etching fusion zone regions (220 DPH) and pulse overlap region between successive melt zones (about 160 DPH) to exceed that of the base metal (120 DPH). The hardness of the fusion boundary region with the base metal was also generally higher than that of the base metal (about 180 DPH vs. 120 DPH). Although the base metal HAZ did exhibit a hardness slightly below that of the base metal (115 DPH), its resistance to fracture during tensile testing likely resulted from its narrow width and associated constraint effects. Longitudinal-weld bend ductility testing revealed fracture initiation and propagation to be associated with the pulse overlap region between the successive melt zones (Fig. 11) and a threshold bending strain only marginally below that of the base metal (11% vs. 14%). It is interesting to note that excepting for differences in the morphology and size of the intermetallic particles and the alpha aluminum matrix, the microstructure of the pulse overlap region between the successive melt zones in the pulsed Nd:YAG laser weld was very similar to the fusion boundary region in the EB welds. This similarity in microstructural constituents appeared to explain the preferential crack initiation in these regions during longitudinal bend testing. The wide differences observed in the threshold bending strain between the EB and the pulsed Nd:YAG laser weld were consistent with the wide variations in the size of these microstructural constituents.

Weld Solidification Behavior

Microstructural characterization described above has shown that the solidification microstructure observed within the fusion zone of EB and pulsed Nd:YAG laser welds in Al-8Fe-2Mo vary widely with respect to alpha aluminum grain morphology and dendrite size, the level of alloying element supersaturation of alpha aluminum dendrites, and the type, size, morphology and population density of second-phase intermetallic particles. Despite such apparently wide variations, the observed weld soli-

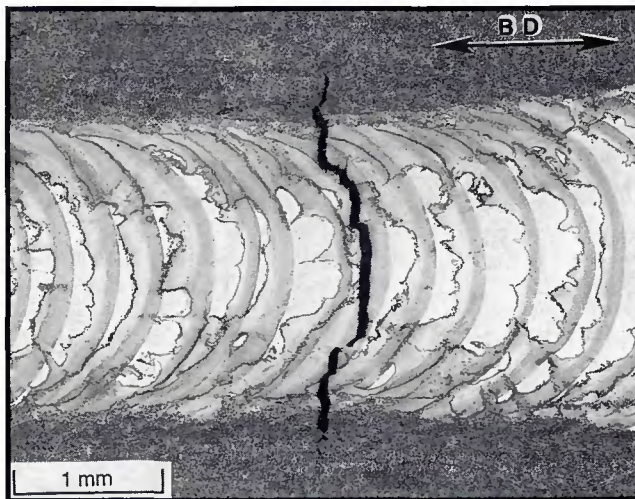


Fig. 11 — Plan view of longitudinal-weld-oriented bend ductility test specimen in Al-8Fe-2Mo showing fracture propagation through the laser weld pulse overlap region between successive melt zones. Arrow indicates bending direction.

dification structures can be broadly classified into three general types:

Type A — Al_3Fe type intermetallic particles in a matrix of dendritic alpha aluminum with interdendritic lamellar or divorced eutectic;

Type B — Al_3Fe type intermetallic particles which act as growth-centers for dendritic alpha aluminum with interdendritic divorced eutectic;

Type C — Al_6Fe type intermetallic particles “entrapped” in a matrix of dendritic alpha aluminum with interdendritic divorced eutectic.

In general, the local mode of fusion zone solidification and resulting microstructure type are dependent on three principal solidification parameters *viz.*, temperature gradient (G_L), solidification velocity (R) and degree of undercooling (ΔT). In this context, the observed variations in the morphology of the primary Al_3Fe type intermetallic particles in the EB weld could be readily attributed to variations in the local temperature gradient obtained in different regions of the weld. Similarly, the observed variations in the size of the alpha aluminum dendrites and the intermetallic particles could be attributed to the variations in the local cooling rate (which is a product of temperature gradient and solidification velocity) with higher cooling rate in pulsed Nd:YAG weld generally producing fine-sized microstructural constituents. Further, the occurrence of lamellar metastable eutectic microstructure in the FBR of the EB weld, and solute-rich particles (*i.e.*, a divorced eutectic) in the dendrite interstices of alpha aluminum in EB and laser welds could be attributed to the local degree of undercooling and the relative size of the interdendritic regions during the terminal stages of weld solidification at these locations (Ref. 15).

The observed variations in the type

and population of intermetallic particles within the weld fusion zone appeared to be related to the peak temperature distribution during fusion welding. Considering that the RS-PM Al-8Fe-2Mo base metal contained both Al_3Fe and Al_6Fe type intermetallic particles in an alpha aluminum matrix, the wide difference in temperature between the melting point of the Al_3Fe type intermetallic particles ($\sim 1150^\circ C$) and the liquidus temperature of the base metal ($\sim 900^\circ C$) likely promoted the occurrence of unmelted or undissolved base metal dispersoid particles in an essentially alpha aluminum melt during the on-heating weld thermal cycle. As shown in Fig. 5A and 5B, fluid flow within the pulsed Nd:YAG weld appeared to control the movement of these dispersoids through the “high” and “low” temperature regions in the weld pool and thereby influence their final size and distribution. These unmelted/undissolved base metal dispersoid particles likely underwent acicular or equiaxed growth during subsequent melt cooling to a degree depending on local thermal condition and weld cooling rate. Under certain conditions of local melt undercooling, these particles likely served as heterogeneous nuclei and thereby promoted separate solidification (*i.e.*, growth) events.

The above considerations show that complete melt homogeneity (characterized by the total absence of unmelted or undissolved base metal dispersoid particles) was not obtained within the bulk fusion zone of EB and pulsed Nd:YAG laser welds. Although the origins of unmelted and undissolved base metal dispersoid particles differ from a physical standpoint, from a metallographic standpoint these particles can not be adequately distinguished. Henceforth, these particles are referred to as undissolved particles.

